Electronic and Thermoelectric Properties of Graphene on 4H-SiC (0001) Nanofacets Functionalized with F4-TCNQ

Chanan Euaruksakul, Hideki Nakajima, Arunothai Rattanachata, Muhammad y Hanna, Ahmad. R. T. Nugraha, Mohamed Boutchich

Electronic and thermoelectric properties of graphene on 4H-SiC (0001) nanofacets functionalized with F4-TCNQ

Chanan Euaruksakul[1], Hideki Nakajima[1], Arunothai Rattanachata[1], Muhammad Y. Hanna[2], Ahmad. R.T. Nugraha[2] and Mohamed Boutchich[3,4]

[1] Synchrotron Light Research Institute, 111 University Avenue, Muang District, Nakhon Ratchasima 30000, Thailand

[2] Research Center for Physics, Indonesian Institute of Sciences (LIPI), Tangerang Selatan, 15314, Indonesia

[3] GeePs | Group of electrical engineering - Paris, CNRS, CentraleSupélec, Univ. Paris-Sud, Université Paris-Saclay, Sorbonne Université, 3 & 11 rue Joliot-Curie, Plateau de Moulon 91192 Gif-sur-Yvette CEDEX, France

[4] CINTRA UMI CNRS/NTU/THALES 3288, Research Techno Plaza, 50 Nanyang Drive, Border X Block, Level 6, Singapore 637553, Singapore

Email: mohamed.boutchich@sorbonne-universite.fr

ABSTRACT

The functionalization of graphene is a well-established route for modulating its optoelectronic properties for a wide range of applications. Here, we studied using photoemission spectroscopies and synchrotron radiation the band structure upon evaporation of a p-type dopant tetrafluoro-tetracyanoquinodimethane (F4-TCNQ) molecules and determined the work function (*WF*) shift over a large area of epitaxial graphene grown on 4H-SiC (0001) silicon carbide substrate. This system exhibits peculiar nanostructures composed of mono and multilayers, notably at the step edges where the electronic properties differ from the terraces. We observed, owing to the high spatial resolution of photoemission electron microscopy (PEEM), that after the adsorption of F4-TCNQ, multilayer graphene on step edges was subjected to less charge transfer as opposed to the monolayer graphene on terraces, making their final *WF* smaller. We calculated the thermoelectric properties of this functionalized graphene system by using density functional theory and Boltzmann transport formalism within the range of the Fermi level (E_F), and the carrier concentration which was

experimentally determined. We show that the *Seebeck* coefficient (*S*) on the nanofacets is 25% larger than on the monolayer terraces, and the maximum power factor (*PF*) is in the order of 10^{-2} W/K^{2}m. This order of magnitude is comparable to the *PF* of commercial thermoelectric material such as bulk bismuth telluride.

Keywords — epitaxial graphene, nanofacets, photoemission spectroscopy, work function, thermoelectric properties.

INTRODUCTION

Graphene grown on silicon carbide (SiC) substrate remains an interesting template for both fundamental studies and applications because it is monolithic to the substrate and does not require any transfer. The synthesized material comprises monolayer graphene on large terraces of several microns in both length and width, and step edges or nanofacets with multilayer graphene ribbons [1,2]. Owing to the tunability of electronic properties, graphene and 2D analogues have been considered to be potential candidates for thermoelectric applications [3–6]. However, in its 2D sheet configuration, graphene presents a thermal conductivity and a zero bandgap that are detrimental for the thermoelectric figure of merit (*ZT*) [7,8]. Interestingly, in a multilayer [9], under specific stacking configuration [10] or patterned into nanoribbons [11,12], owing to confinement effects, graphene exhibits a finite bandgap [13]. Moreover, these structures, when functionalized by heteroatoms, undergo substantial variation of their electronic and thermal properties. The doping level can be tailored to increase the electrical conductivity (σ) and hence the *PF*. The ambipolar transport in graphene implies positive (holes) or negative (electrons) *S* coefficients adjusting the E_F position by chemical doping or field-effect gating [14]. Therefore, E_F can then be located anywhere in the electron dispersion spectra of graphene yielding to *n*- or *p*-type material. This feature allows unipolar carrier transport that prevents *S* being compensated for by the contribution of both carrier types. *WF* and barrier height at the interface of a heterostructure are modulated, and the carrier injection mechanism can be judiciously controlled. There have been numerous studies on the functionalization of monolayer graphene using various adsorbates, notably F4-TCNQ, an effective *p*-type dopant [15,16]. This molecule is a strong electron acceptor that compensates for the natural *n*-type doping of

pristine graphene grown on SiC substrates. Much less work has focused on the electronic properties at the step edges or nanofacets. These nanostructures, which exhibit a structure different from the terraces, cannot be effectively probed using spatially averaged techniques [17,18]. Angle-resolved photoemission electron spectroscopy (ARPES) is a powerful tool that reveals the electron-dispersion spectrum as well as the overall impact of any adsorbate onto graphene [19]. However, it is not possible to isolate the local electronic variations with a typical micron size probe of ~ 100 μm. On the other hand, PEEM provides localized information as well as the topography of the material.

In this work, we have investigated functionalized epitaxial graphene on SiC and probed its electronic properties at the step edges using PEEM mapping. We determined that the *WF* variation between the step edges and monolayer terraces is as high as 0.7 eV after doping. We calculated *S* and σ within the range of the experimental E_F and carrier density achieved and estimated the resulting *PF* for both monolayer terrace and the nanofacets. The results showed an optimum *S* ~ 100 μV/K and S ~125 μV/K for monolayer and bilayer graphene, respectively with a *PF* of ~ 10^{-2} W/K^{2}m.

EXPERIMENTAL

Materials

The graphene was grown on *n*-type 4H-SiC (0001) substrates. The substrate was first heated to 1000 °C in an ultra-high vacuum (UHV) chamber and up to 1525 °C in an argon (Ar) atmosphere to favour the formation of a large and homogeneous graphene layer. The sample was then cooled from 1525 °C to room temperature. A homogenous topography showed several ~ μm wide terraces on average, separated by step edges [1,3]. The F4 – TCNQ molecules with 97% purity were sourced from Sigma-Aldrich. The material was placed in a crucible in an *in-situ* effusion cell fitted to the ARPES and PEEM systems.

Instrumentations and measurements

The band structure of the sample was measured around the K-point of the graphene Brillouin zone (BZ) using a synchrotron radiation-based ARPES beamline 3.2Ua: PES of the Synchrotron Light Research Institute (SLRI). The spectra were averaged over a 100 μm^2 probe diameter and acquired using a Scienta R4000 analyzer. The sample was placed in the 6-axis manipulator at room

temperature at a photon energy of 40 eV with an energy resolution of ~ 130 meV [20]. PEEM was performed at the beamline 3.2Ub:PEEM with an Elmitec LEEM PEEM III [21]. The imaging electron energy analyzer was utilized for the *WF* mapping and micro-XPS (the description of *WF* mapping by PEEM is provided in the Supplementary Material). The *in-situ* LaB_6 electron gun was used as a source for low-energy electron microscopy (LEEM). PEEM and LEEM could be switched so that the analyses by both techniques could be carried out on the same microscopic area. The *WF* mapping in PEEM was measured at 110 eV photon energy.

Graphene on *n*-type 4H-SiC (0001) was degassed at 400 °C overnight and then left to cool to room temperature. After the degassing, the graphene layer was checked by LEEM, LEED and XPS for its structural integrity and cleanliness. F4-TCNQ was then evaporated from a low-temperature effusion cell (NTEZ - MBE Komponenten). The material was degassed at ~ 80 °C in a quartz crucible and for a few hours while the gate valve was closed. The temperature was then raised to 100 °C for the deposition, and when the gate valve opened, the pressure in the analysis chamber rose from ~ 10^{-10} mbar to low 10^{-9} mbar. The distance from the crucible lip to the sample is approximately 25 cm in the PEEM chamber and 10 cm in the ARPES chamber. *In-situ* LEEM observation during F4-TCNQ deposition and XPS result after the deposition are shown in supplementary Figures SI 1&2.

The near-edge X-ray absorption fine structure (NEXAFS) was measured at the ARPES chamber in the total electron yield mode, which monitors the drain current from the sample as a function of the photon energy over the nitrogen K edge. The energy resolution of the NEXAFS N K edge is 0.4 eV.

RESULTS AND DISCUSSION

Figure 1 shows the Raman spectrum of the *as*-deposited sample. For clarity, the SiC Raman signature has been subtracted to reveal the main features of graphene G ~ 1570 cm-1 and 2D ~ 2700 cm^{-1}. The D peak ~ 1350 cm^{-1} could be assigned to structural defects, such as Si clusters from broken Si-C bonds that are typically formed during the high-temperature graphitization.

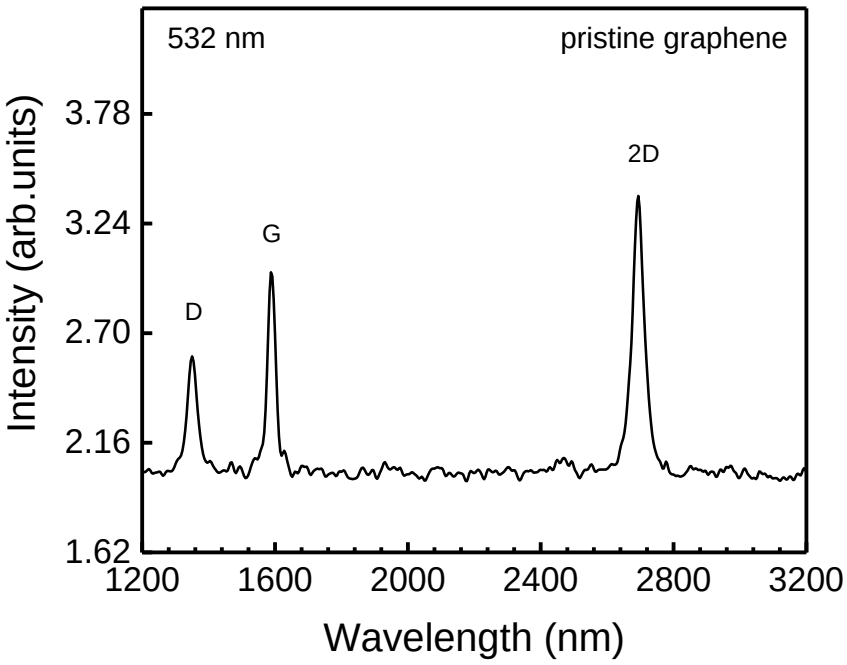

Fig. 1. Raman spectrum of as-grown graphene. The presence of the G and 2D bands across the overall area indicates homogeneous growth of graphene, but a D peak indicates the presence of defects.

Photoemission characterization

Figure 2a displays a LEEM image of graphene on 4H-SiC (0001) and the intensity-voltage (I-V) profiles on different marked areas. The number of dips in the I-V profiles correlates with the number of graphene layers [22]. In Figure 2, for the 10 µm field of view (start voltage = 3.8 eV), there are three different domains with one, two and three dips in the I-V curves, which indicates that the domains are monolayer, bilayer and trilayer graphene, respectively.

(a)

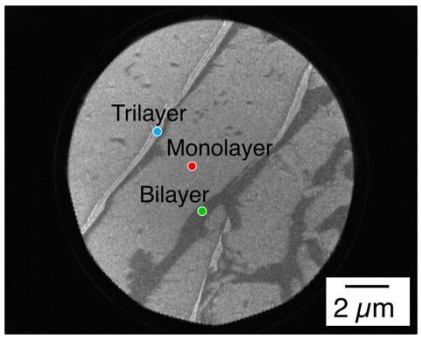

(b)

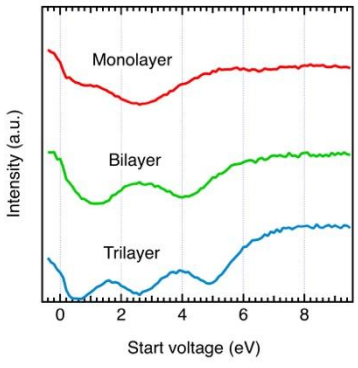

Fig. 2. a) LEEM image at the start voltage of 3.8 eV showing flat terraces with monolayer graphene and strips representing nanofacets containing bilayer and trilayer graphene. b) LEEM-IV curves of graphene before F4-TCNQ deposition. The number of dips in each plot corresponds to the number of graphene layers.

The LEEM image indicates that 76% of the area comprises monolayer graphene, whereas the bilayer and trilayer graphene occupy approximately 17% and 7% of the total area, respectively. These bilayer and trilayer graphene appear as narrow ribbons above the nanofacets all over the surface [23] of SiC substrate, where graphene grows thicker near kinks and defects [24,25]. Figure 3a shows the electron dispersion $E(k)$ for the pristine sample along the perpendicular to the ΓK graphene Brillouin zone, with a residual *n*-type doping with E_F lying at ~ 0.43 eV above the Dirac point E_D yielding a charge carrier concentration of $n \sim 1.36 \times 10^{13}$ cm^{-2}. Figure 3(b–d) represent the *E(k)* for the doped sample with an increasing number of molecules while the spectra are accumulated.

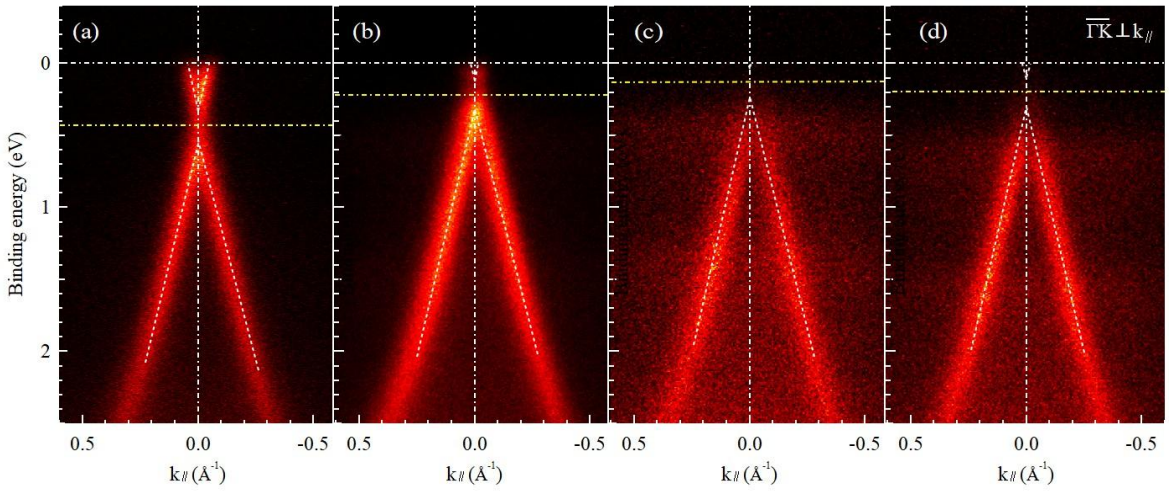

Fig. 3. ARPES measurement of graphene/4H-SiC (0001). (a) Pristine graphene, (b) after heating and opening the shutter, (c) after 2 min of deposition and (d) after 12 min. Spectra were recorded continuously. Table I shows the F4 TCNQ coverage and the carrier concentrations calculated from these ARPES plots (see supplementary Figs. SI3 and SI4 for detailed evaluation of E_D)**.**

As displayed in figure 3 (b–d), E_F shifts downward towards E_D, implying a charge transfer of holes into the graphene compensating the initial *n*-type doping; the E_F - E_D ~ 0.13 eV. However, beyond 0.74 nm of molecules estimated from the angle-resolved XPS (N1s, F1s and Si2p) and the attenuation

length of Si2p, the charge transfer saturates, and E_F - E_D ~ 0.2 eV. The ARPES clearly reveals the charge transfer and the relative change in E_F and therefore the *WF*. The charge-carrier concentration *n* was derived from the slope of the *E(k)* branches [15,26], Table I. The flat bands distributed at 0.5–0.7 and 1.3–1.5 eV in Fig. 3(c–d) correspond to the partially filled lowest-unoccupied molecular orbital (LUMO) and relaxed highest-occupied molecular orbital (HOMO) of F4-TCNQ resulting from the electron transfer [27,28], respectively.

	a	**b**	**c**	**d**
Deposition time (min)	**pristine**	**0**	**2**	**12**
F4-TCNQ (nm)	0	0.58	0.74	0.74
Dirac point (eV)	0.43	0.22	0.13	0.2
Carrier concentration (10^{12} cm $^{-2}$)	13.6	3.55	1.24	2.94

Table I: Dirac point and charge carrier concentration for each deposition time of F4 TCNQ.

Figure 4 shows the near edge X-ray absorption fine structure (NEXAFS) of the nitrogen K edge on F4-TCNQ/graphene (corresponding to the panel Fig. 3d conditions). The NEXAFS spectra were measured in the total electron yield mode with three different incident angles of linearly polarized light. The angular dependence of peaks observed in the energy range below 404 eV resulted from the molecular orientation of F4-TCNQ on the graphene substrate.

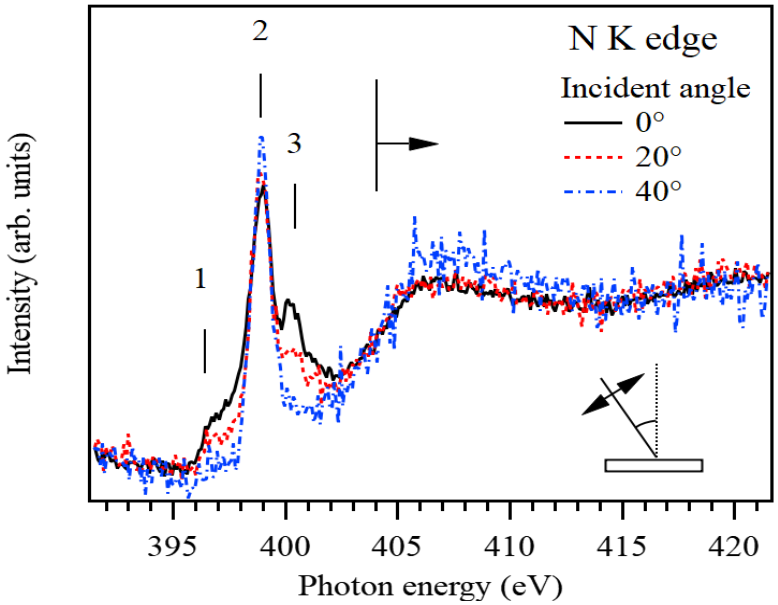

Fig. 4. Angular-dependent N K edge NEXAFS spectra of F4-TCNQ on graphene measured for different incidence angles of the linear polarized synchrotron light (θ = 0°, 20° and 40°). Inset

illustrates the NEXAFS geometry: θ represents the angle between the polarization vector $\vec{E}$ and the surface normal $\vec{n}$.

The first peak located at 396.5 eV decreases as the incident angle increases, and the second peak located at 399.0 eV shows the highest intensity and slightly increases. The third peak located at 400.5 eV decreases as the incident angle increases. These three peaks are well characterized in their orbitals and symmetries [29]. The first peak corresponds to π* (a_u, b_{1u}), and the second peak consists of π* (b_{3g}, a_u) and σ*(b_{1g}, b_{2u}). The third peak originates from π* (b_{2g}). The π* orbital is distributed out of the F4-TCNQ molecular plane, whereas σ* has an orbital in the molecular plane. Because resonances 1 and 3 are clearly observed at the normal incidence, one can assert that the molecules stand upright on the terraces, in agreement with the literature [15]. Resonance 2 has two different features close to each other; the intensity does not significantly change with the light polarization, as opposed to the 2 other resonances. The broad peak above 404 eV is assigned to σ* orbitals, and the ionization threshold is located at 404 eV. XPS analysis of the N1s peak shows the presence of anionic and neutral configurations in supplementary Figure SI1. N1s can be deconvoluted into 3 peaks by Gaussian fitting after background subtraction. The first peak located at 397.7 eV corresponds to the anionic species N^{-1}, and the second peak located at 399.6 eV is attributed to the neutral N^0 species. The third peak appears at 401.5 eV and seems to be the satellite peak due to the shake-up process [30,31]. The anionic species contribute to the charge transfer through the C≡N bonds, whereas the fluorine atoms remain inactive. F1s spectra (supplementary Fig. SI1) present no difference independently of the deposition conditions. The XPS results agree with the literature and support the standing-upright orientation of F4-TCNQ molecules on the graphene substrate, a result that is also consistent with our NEXAFS results. Note that it is not possible using NEXAFS to resolve the nanofacets, but we believe (considering the tilted topography) that the molecules could be lying down, which is the most energetically stable position, as calculated by Tian *et al.* [32].

Furthermore, we observed the non-homogeneous modification of electronic structure for graphene functionalized with F4-TCNQ by *WF* mapping under PEEM, Fig. 5. Whereas the F4-TCNQ deposition in PEEM was made on a separate setup from the PES platform, the deposition parameters

were identical. This ensured that F4- TCNQ molecules deposited in PEEM were in the same configuration and induced a similar effect on the electronic properties. Note that the absolute *WF* measurement in PEEM is tedious to perform directly due to both non-isochromaticity in the imaging XPS mode and the difficulty in determining the Fermi edge. To evaluate the absolute *WF* profile of pristine graphene (blue line) in Fig. 5c, the PEEM measurement before functionalization was offset by the absolute *WF* ~ 4.3 eV of the monolayer graphene measured in our previous work [1,3]. After F4-TCNQ deposition, we offset the PEEM data by the positive shift of 1.28 eV on monolayer graphene measured by PES (our *WF* shift measurement originated mostly from monolayer domains, which covered more than 76% of the surface, and the result also compares well with Chen *et al.* [28] and Coletti et *al.* [15] who reported shifts of *WF* for monolayer graphene on 6H-SiC(0001) after F4-TCNQ deposition of 1.3 eV and 1 eV, respectively).

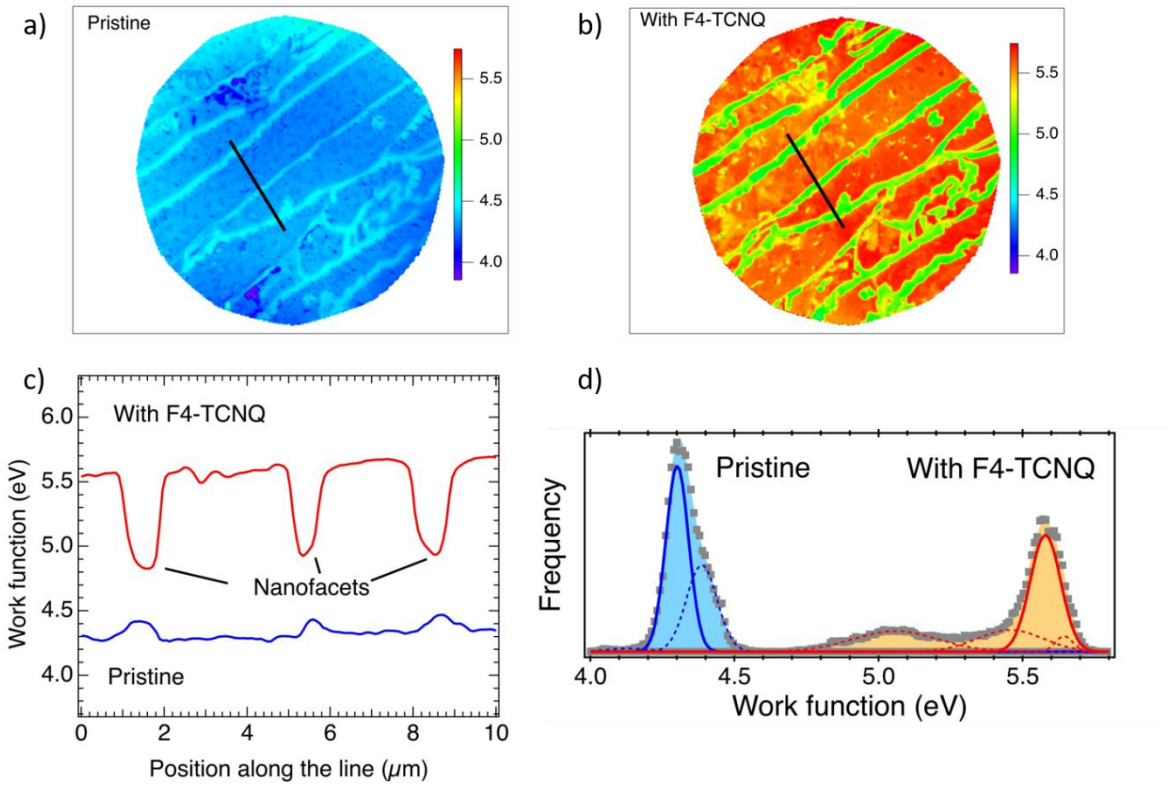

Fig. 5. Work function mapping before (a) and after (b) F4-TCNQ deposition on graphene/SiC (25 μm field of view). (c) line profiles showing work function variation across graphene on terraces and on nanofacets of SiC. d) Histograms showing the distribution of work function from work function mapping in (a) and (b).

In the 25 μm field of view and before the onset of deposition (Fig. 5a), we observed a small *WF* difference between graphene on the terraces (monolayer) and nanofacets (bilayer and trilayer), which exhibit a ~ 0.1 eV larger *WF* than the monolayer areas. This observation has been reported on 6H-SiC(0001) by Hibino *et al*. [33] and on 6H-SiC(000$\bar{1}$) by Mathieu *et al.* [34,35]. We also noted smaller domains within monolayer graphene scattered all over the SiC terraces, which have slightly lower (less than 0.1 eV) *WF*. Figure 5b displays the mapping after 8-minute deposition of F4-TCNQ. The *WF* profile dramatically changed, as shown by the line profiles in Fig. 5c. The *WF* of monolayer graphene on SiC terraces became ~ 0.7 eV larger than the graphene on top of nanofacets, as shown by the red line profile in Fig. 5c. The profile shows that electron transfer occurs strongly on the monolayer graphene on SiC terraces and, in contrast, there is a relatively much smaller effect induced by F4-TCNQ on bilayer and trilayer graphene domains on the nanofacets, where the *WF* shifts only by ~ 0.5-0.6 eV. This functionalization also makes the *WF* of the bilayer and trilayer graphene domains smaller than the monolayer graphene after F4-TCNQ doping. To provide a statistical representation of the work function changes under the entire field of view in Fig. 5a and 5b, histograms of the *WF* data from individual pixels of the *WF* mapping before and after F4-TCNQ deposition are plotted together in Fig. 5d. Each histogram is fitted with Gaussian functions to determine the number of species distinguishable by a small difference in *WF* [34,36]. The main peaks before and after F4-TCNQ deposition (solid blue and red lines) represent the monolayer graphene on SiC terraces that covers most of the total surface area. The histogram shows the overall shifts over the entire area and a clear spreading of the work function over a wider range after doping by F4-TCNQ. Shoulders are observed on both lower and higher energies of the main peak centred at 5.5 eV. This also shows up as a non-uniform colour for the monolayer graphene domains in the mapping and could be assigned to either the non-uniform layer of F4-TCNQ or interactions with the buffer layer at the substrate interface. Note that the large full width half maximum (FWHM) of the Gaussian peaks that represent the bilayer and trilayer graphene (at 0.53 eV lower than the main monolayer graphene) in the histogram are assigned to the artefacts inherent to the small electric field on the surface of the sample arising from the difference in *WF* itself [37].

To discuss the difference in charge transfers of F4-TCNQ that results in different shifts of *WF* on monolayer graphene on terraces, and bilayer and trilayer graphene on nanofacets, we compared our results with the literature. F4-TCNQ may adsorb on graphene with either standing or lying-down configurations depending on the types of supporting substrates [38,39] and the surface coverage. For F4-TCNQ on epitaxial monolayer graphene on SiC, the molecules lie down parallel to the surface at low coverage [40]. At high coverage, the configuration switches to standing upright with the cyano groups of F4-TCNQ bonding to the surface only on one side. This configuration change is evidenced by the deconvolution of N 1s spectra in XPS into N^{-1} and N^{0} components [6,15] and by angular-dependent NEXAFS in this work (which largely measures the monolayer graphene). To our knowledge, there is no report on the determination of the adsorption configurations of F4-TCNQ on pure bi-layer graphene on SiC. We could not clarify the orientation of the molecules on the narrow nanofacets, neither by NEXAFS nor by PEEM, due to the angle rotation constraints of our equipment. However, DFT calculations by Tian *et al.* [32] have shown that the F4-TCNQ molecule lies down on free-standing bi-layer graphene [32], and this is likely to occur on the bilayer and trilayer graphene near the nanofacets. Although it is expected that lying down F4-TCNQ induces more charge transfer per molecule (they transfer electrons with the cyano groups on both sides instead of on one side), the adsorption footprint in this configuration is larger, and there could be repulsive forces between the molecules that makes the packing less dense compared to that of standing F4-TCNQ on monolayer graphene; hence, a lower *WF* shift is observed on the nanofacets.

Evaluation of thermoelectric properties

Functionalized graphene superlattices are thought to enhance the TE properties [41]. Considering the electronic properties measured on our graphene template functionalized with F4-TCNQ, we determined the TE properties of monolayer and bilayer graphene within the linear Boltzmann transport theory and constant relaxation time approximation (CRTA). In this framework, one can calculate S and σ assuming a phenomenological relaxation time constant τ_0 and electronic energy dispersion $E_{s\mathbf{k}}$, where s denotes the band index and $\boldsymbol{k}$ is the electron wave vector. The electronic structure of the functionalized graphene is calculated using Quantum ESPRESSO [42,43]. We carried out a geometrical optimization for the orientation of the molecule and found that the most stable

configuration on both monolayer, bilayer and trilayer graphene was the F4-TCNQ molecule lying down above graphene. The expressions for S and σ are[3–5,44–46]

$$S = -\frac{1}{eT}\frac{\sum_{s,\mathbf{k}}(E_{s\mathbf{k}}-E_F)v_{s\mathbf{k}}^2\tau_0\frac{\partial f_{s\mathbf{k}}}{\partial E_{s\mathbf{k}}}}{\sum_{s,\mathbf{k}}v_{s\mathbf{k}}^2\tau_0\frac{\partial f_{s\mathbf{k}}}{\partial E_{s\mathbf{k}}}}, \quad (1)$$

and

$$\sigma = -\frac{e^2}{NV}\sum_{s,\mathbf{k}}v_{s\mathbf{k}}^2\tau_0\frac{\partial f_{s\mathbf{k}}}{\partial E_{s\mathbf{k}}}, \quad (2)$$

where e is the unit electric charge (defined to be positive), T is the average temperature of the material, N is the number of $\boldsymbol{k}$ in the unit cell, E_F is the Fermi energy, $f_{s\mathbf{k}}$ is the Fermi-Dirac distribution function and $v_{s\mathbf{k}}$ is the component of the electronic group velocity for a specific direction at each $\boldsymbol{k}$ point. Note that the CRTA is valid for near-equilibrium transport involving elastic and isotropic scattering, which we assume in this work for simplicity. Figure 6 illustrates the model implemented. The accuracy of the calculation thus mostly depends on the choice of τ_0 parameter, which can be measured experimentally or taken from the literature. Figure 7 presents the calculated results of S, σ and PF (which is equal to $S^2\sigma$) for the functionalized monolayer and bilayer graphene as a function of Fermi energy and the carrier concentration. For each thermoelectric quantity, there are two curves shown in Figure 7 scaled with E_F and the carrier concentration, respectively for the experimental doping range achieved. The plots of σ and PF are scaled by τ_0, where the value of this τ_0 parameter could vary depending on the sample, typically on the order of 0.5–10 ps as observed by pump probe techniques [47,48]. Note that from the formulas of S and σ, S does not depend on the relaxation time because τ_0 in the numerator will cancel with that in the denominator, as opposed to σ.

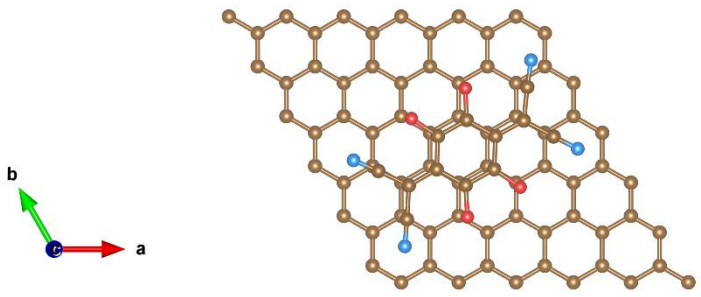

Fig. 6. F4TCNQ on free-standing graphene configuration after relaxation. The molecule is in a lie-down position, which is the most energetically favourable configuration for both low and high coverage.

In Figure 7, the maximum S values are close to 100 μV/K for functionalized monolayer graphene, whereas bilayer graphene exhibits a S ~125 μV/K that is higher than that of monolayer graphene owing to the bandgap opening. This order of magnitude is on par with experimental data [14,49] measured on flakes. We observe that upon appropriate doping within –0.5 to 0.5 eV or with a carrier concentration of the order of 10^{12} cm^{-2}, which we attained experimentally (see Table I), the TE properties of graphene could be enhanced significantly. There exists an optimal doping to obtain the maximum PF in both p- and n-type graphene, where the p-type (n-type) corresponds to the negative (positive) E_F or the positive (negative) carrier concentration. The presence of two maximum peaks in PF near $E_F = 0$ is mainly due to the two peaks (negative and positive) S because the electrical conductivity monotonically increases with doping. However, the values of maximum PF strongly depend on the relaxation time τ_0. Using Figure 7, and knowing τ_0 and the carrier concentration, one can estimate the thermoelectric properties of one's own functionalized graphene sample. For example, we can estimate by assuming the typical relaxation time within 0.5–10 ps, the maximum calculated PF in the order of 10^{-2} W/K^2m, which is in the same order of magnitude as the PF of bulk bismuth telluride [50], one of the most integrated TE materials available on the market. Functionalization or doping of graphene multilayer nanofacets exhibit enhanced thermoelectric performance. Practically, one would need to isolate the graphene patterns from the substrate to reduce heat losses.

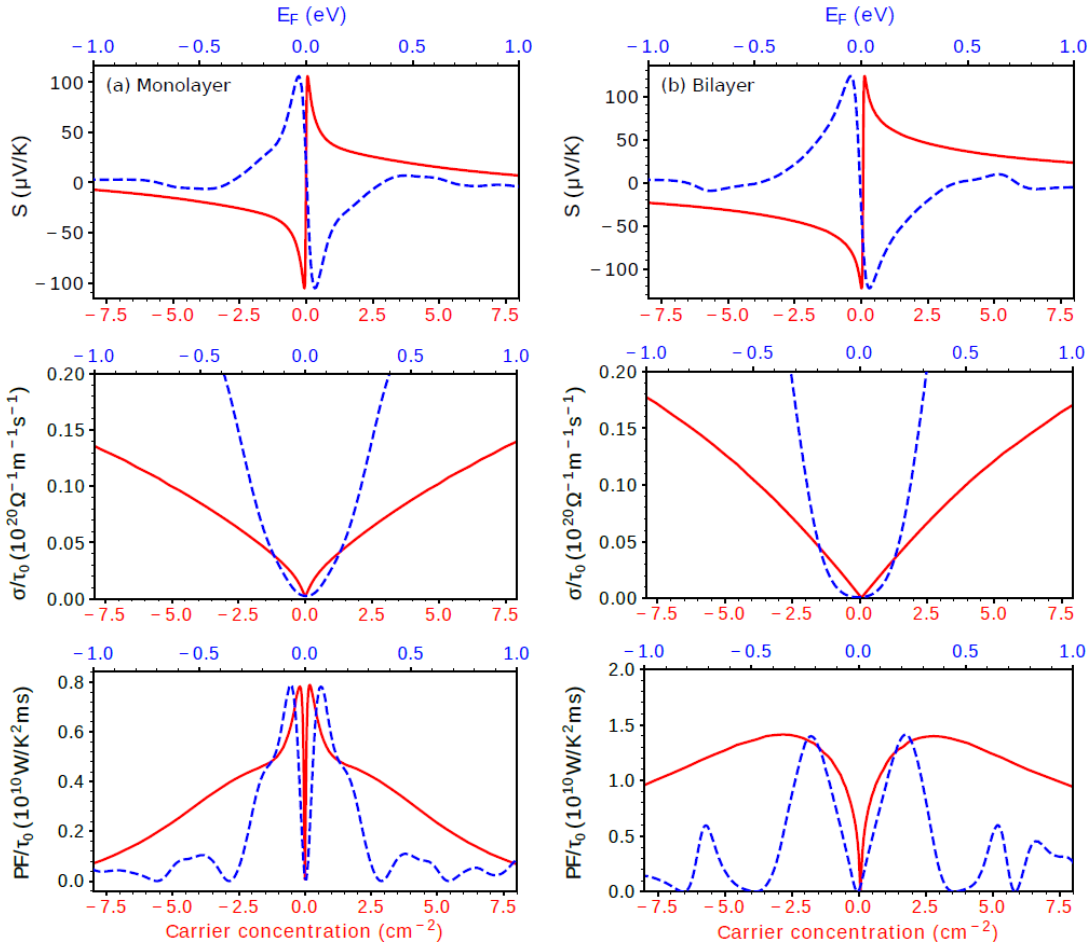

Fig. 7. Calculated Seebeck coefficient, electrical conductivity and power factor as a function of Fermi energy (upper horizontal axis) and carrier concentration (lower horizontal axis) for (a) monolayer and (b) bilayer graphene. Note that the electrical conductivity and power factor are scaled by the relaxation time. The range of Fermi energy in this figure covers a larger range of doping than the range of carrier concentration. The blue trace is scaled with E_F, whereas the red one with the carrier concentration.

CONCLUSION

Substrate-graphene interaction always plays an important role in determining the electronic structure of graphene. In this work, we demonstrated that surface-transfer doping is also affected by different graphene thicknesses, particularly on the nanofacet structures of the substrate. This difference results in non-homogeneous charge transfers across the graphene layer. This inhomogeneity may either be detrimental to device performance or, on the other hand, be used as a bottom-up approach to control the energy level and create different graphene electronic structures suitable for TE applications. Here, we observed a direct change in the electronic properties and band structure of graphene upon *in-situ* functionalization by F4-TCNQ molecules. We have also mapped the *WF* across the sample and

observed a significant difference in the charge transfers from F4-TCNQ doping on the monolayer graphene on terraces as opposed to bilayer and trilayer graphene on nanofacets. Considering the electronic properties measured under the synchrotron beamline and a relaxation time range 0.5–10 ps, we obtained a maximum thermoelectric power factor *PF* in the order of 10^{-2} W/K^2m, comparable to commercial thermoelectric materials. Interestingly, we observed that the graphene on nanofacets located at the edges exhibits a *PF* nearly as high as the monolayer graphene on the terraces and a *Seebeck* coefficient 25 % larger. This improvement suggests that functionalization is an effective route to enhance the thermoelectric properties of nanostructured materials.

ACKNOWLEDGMENT

The authors would like to thank Dr Abdelkarim Ouerghi for providing high quality epitaxial graphene samples. M.B. would like to thank the Centre National de la Recherche Scientifique (CNRS) for their financial support through the JRP program grant number 1630 as well as Professor Songphol Kanjanachuchai (Chulalongkorn University) for fruitful discussions. M.Y.Y. and A.R.T.N. acknowledge Mahameru Grid LIPI for their high-performance computing facilities. C.E. would like to thank Pat Photongkam and Thipusa Wongpinij for assisting in LEEM/PEEM operations.

REFERENCES:

1. M. Boutchich, H. Arezki, D. Alamarguy, K.-I. Ho, H. Sediri, F. Gunes, Fethullah, J. Alvarez, J. Kleider, C. Lai, and A. Ouerghi, Appl. Phys. Lett. **105**, 233111 (2014).
2. E. Pallecchi, F. Lafont, V. Cavaliere, F. Schopfer, D. Mailly, W. Poirier, and A. Ouerghi, Sci Rep **4**, 4558 (2014).
3. F. Günes, H. Arezki, D. Pierucci, D. Alamarguy, J. Alvarez, J.-P. Kleider, Y. J. Dappe, A. Ouerghi, and M. Boutchich, Nanotechnology **26**, 445702 (2015).
4. Z. Han, A. Kimouche, D. Kalita, A. Allain, H. Arjmandi-Tash, A. Reserbat-Plantey, L. Marty, S. Pairis, V. Reita, N. Bendiab, J. Coraux, and V. Bouchiat, Adv. Funct. Mater. **24**, 964 (2014).
5. K.-I. Ho, M. Boutchich, C.-Y. Su, R. Moreddu, E. S. R. Marianathan, L. Montes, and C.-S. Lai, Adv. Mater. **27**, 6519 (2015).
6. L. Khalil, D. Pierucci, E. Papalazarou, J. Chaste, M. G. Silly, F. Sirotti, M. Eddrief, L. Perfetti, E. Lhuillier, and A. Ouerghi, Phys. Rev. Mater. **3**, 084002 (2019).
7. T. A. Amollo, G. T. Mola, M. S. K. Kirui, and V. O. Nyamori, Crit. Rev. Solid State Mater. Sci. **43**, 133 (2018).
8. V.-T. Tran, J. Saint-Martin, P. Dollfus, and S. Volz, Sci. Rep. **7**, 2313 (2017).
9. L. I. Johansson, R. Armiento, J. Avila, C. Xia, S. Lorcy, I. A. Abrikosov, M. C. Asensio, and C. Virojanadara, Sci. Rep. **4**, 4157 (2015).

10. W. Bao, L. Jing, J. Velasco, Y. Lee, G. Liu, D. Tran, B. Standley, M. Aykol, S. B. Cronin, D. Smirnov, M. Koshino, E. McCann, M. Bockrath, and C. N. Lau, Nat. Phys. **7**, 948 (2011).
11. K.-P. Chang, K.-I. Ho, M. Boutchich, julien chaste, H. Arezki, and C.-S. Lai, Semicond. Sci. Technol. **35**, 015005 (2019).
12. T. Fang, A. Konar, H. Xing, and D. Jena, Phys. Rev. B **78**, 205403 (2008).
13. E. H. Hasdeo, L. P. A. Krisna, M. Y. Hanna, B. E. Gunara, N. T. Hung, and A. R. T. Nugraha, J. Appl. Phys. **126**, 035109 (2019).
14. Y. M. Zuev, W. Chang, and P. Kim, Phys. Rev. Lett. **102**, 096807 (2009).
15. C. Coletti, C. Riedl, D. S. Lee, B. Krauss, L. Patthey, K. Von Klitzing, J. H. Smet, and U. Starke, Phys. Rev. B **81**, 235401 (2010).
16. H. Pinto, R. Jones, J. P. Goss, and P. R. Briddon, J. Phys. Condens. Matter **21**, 402001 (2009).
17. C. Chen, J. Avila, H. Arezki, F. Yao, V. L. Nguyen, Y. H. Lee, M. Boutchich, and M. C. Asensio, J. Phys. Conf. Ser. **864**, 012029 (2017).
18. H. Henck, Z. Ben Aziza, D. Pierucci, F. Laourine, F. Reale, P. Palczynski, J. Chaste, M. G. Silly, F. Bertran, P. Le Fèvre, E. Lhuillier, T. Wakamura, C. Mattevi, J. E. Rault, M. Calandra, and A. Ouerghi, Phys. Rev. B **97**, 155421 (2018).
19. P. Ayria, S. Tanaka, A. R. T. Nugraha, M. S. Dresselhaus, and R. Saito, Phys. Rev. B **94**, 075429 (2016).
20. H. Nakajima, A. Tong-on, N. Sumano, K. Sittisard, S. Rattanasuporn, C. Euaruksakul, R. Supruangnet, N. Jearanaikoon, P. Photongkam, N. Chanlek, and P. Songsiriritthigul, J. Phys. Conf. Ser. **425**, 132020 (2013).
21. C. Euaruksakul, N. Jearanaikoon, W. Bussayaporn, N. Kamonsutthipaijit, P. Photongkam, S. Tunmee, and P. Songsiriritthigul, J. Phys. Conf. Ser. **425**, 182011 (2013).
22. H. Hibino, H. Kageshima, F. Maeda, M. Nagase, Y. Kobayashi, and H. Yamaguchi, Phys. Rev. B - Condens. Matter Mater. Phys. **77**, 075413 (2008).
23. D. Pierucci, H. Sediri, M. Hajlaoui, E. Velez-Fort, Y. J. Dappe, M. G. Silly, R. Belkhou, A. Shukla, F. Sirotti, N. Gogneau, and A. Ouerghi, Nano Res. **8**, 1026 (2015).
24. M. L. Bolen, S. E. Harrison, L. B. Biedermann, and M. A. Capano, Phys. Rev. B **80**, 115433 (2009).
25. J. Osaklung, C. Euaruksakul, W. Meevasana, and P. Songsiriritthigul, Appl. Surf. Sci. **258**, 4672 (2012).
26. S. Y. Zhou, G.-H. Gweon, A. V. Fedorov, P. N. First, W. A. de Heer, D.-H. Lee, F. Guinea, A. H. Castro Neto, and A. Lanzara, Nat. Mater. **6**, 770 (2007).
27. N. Koch, S. Duhm, J. P. Rabe, A. Vollmer, and R. L. Johnson, Phys. Rev. Lett. **95**, 237601 (2005).
28. W. Chen, S. Chen, D. C. Qi, X. Y. Gao, and A. T. S. Wee, J. Am. Chem. Soc. **129**, 10418 (2007).
29. J. Fraxedas, Y. J. Lee, I. Jiménez, R. Gago, R. M. Nieminen, P. Ordejón, and E. Canadell, Phys. Rev. B - Condens. Matter Mater. Phys. **68**, 195115 (2003).
30. J. M. Lindquist and J. C. Hemminger, J. Phys. Chem. **92**, 1394 (1988).
31. P. Persson, S. Lunell, A. Szöke, B. Ziaja, and J. Hajdu, Protein Sci. **10**, 2480 (2009).
32. X. Tian, J. Xu, and X. Wang, J. Phys. Chem. B **114**, 11377 (2010).
33. H. Hibino, H. Kageshima, M. Kotsugi, F. Maeda, F.-Z. Guo, and Y. Watanabe, Phys. Rev. B **79**, 125437 (2009).
34. C. Mathieu, N. Barrett, J. Rault, Y. Y. Mi, B. Zhang, W. A. De Heer, C. Berger, E. H. Conrad, and O. Renault, Phys. Rev. B - Condens. Matter Mater. Phys. **83**, 235436 (2011).
35. J. Hicks, A. Tejeda, A. Taleb-Ibrahimi, M. S. Nevius, F. Wang, K. Shepperd, J. Palmer, F. Bertran, P. Le Fèvre, J. Kunc, W. A. De Heer, C. Berger, and E. H. Conrad, Nat. Phys. **9**, 49 (2013).

373 36. N. Barrett, O. Renault, H. Lemaître, P. Bonnaillie, F. Barcelo, F. Miserque, M. Wang, and
374 C. Corbel, J. Electron Spectrosc. Relat. Phenom. **195**, 117 (2014).
375 37. J. Jobst, L. M. Boers, C. Yin, J. Aarts, R. M. Tromp, and S. J. van der Molen,
376 Ultramicroscopy **200**, 43 (2019).
377 38. S. Yoshimoto, K. Kameshima, T. Koitaya, Y. Harada, K. Mukai, and J. Yoshinobu, Org.
378 Electron. **15**, 356 (2014).
379 39. H.-Z. Tsai, A. A. Omrani, S. Coh, H. Oh, S. Wickenburg, Y.-W. Son, D. Wong, A. Riss,
380 H. S. Jung, G. D. Nguyen, G. F. Rodgers, A. S. Aikawa, T. Taniguchi, K. Watanabe, A. Zettl,
381 S. G. Louie, J. Lu, M. L. Cohen, and M. F. Crommie, ACS Nano **9**, 12168 (2015).
382 40. W. Chen, D. Qi, X. Gao, and A. T. S. Wee, Prog. Surf. Sci. **84**, 279 (2009).
383 41. J. Y. Kim and J. C. Grossman, Nano Lett. **15**, 2830 (2015).
384 42. P. Giannozzi, S. Baroni, N. Bonini, M. Calandra, R. Car, C. Cavazzoni, D. Ceresoli, G. L.
385 Chiarotti, M. Cococcioni, I. Dabo, A. Dal Corso, S. De Gironcoli, S. Fabris, G. Fratesi, R.
386 Gebauer, U. Gerstmann, C. Gougoussis, A. Kokalj, M. Lazzeri, L. Martin-Samos, N. Marzari,
387 F. Mauri, R. Mazzarello, S. Paolini, A. Pasquarello, L. Paulatto, C. Sbraccia, S. Scandolo, G.
388 Sclauzero, A. P. Seitsonen, A. Smogunov, P. Umari, and R. M. Wentzcovitch, J. Phys.
389 Condens. Matter **21**, 395502 (2009).
390 43. P. Giannozzi, O. Andreussi, T. Brumme, O. Bunau, M. Buongiorno Nardelli, M. Calandra,
391 R. Car, C. Cavazzoni, D. Ceresoli, M. Cococcioni, N. Colonna, I. Carnimeo, A. Dal Corso, S.
392 de Gironcoli, P. Delugas, R. A. DiStasio, A. Ferretti, A. Floris, G. Fratesi, G. Fugallo, R.
393 Gebauer, U. Gerstmann, F. Giustino, T. Gorni, J. Jia, M. Kawamura, H.-Y. Ko, A. Kokalj, E.
394 Küçükbenli, M. Lazzeri, M. Marsili, N. Marzari, F. Mauri, N. L. Nguyen, H.-V. Nguyen, A.
395 Otero-de-la-Roza, L. Paulatto, S. Poncé, D. Rocca, R. Sabatini, B. Santra, M. Schlipf, A. P.
396 Seitsonen, A. Smogunov, I. Timrov, T. Thonhauser, P. Umari, N. Vast, X. Wu, and S. Baroni,
397 J. Phys. Condens. Matter **29**, 465901 (2017).
398 44. H. J. Goldsmid, *Introduction to Thermoelectricity* (Springer, Berlin, 2009).
399 45. B. Liao, J. Zhou, B. Qiu, M. S. Dresselhaus, and G. Chen, Phys. Rev. B - Condens.
400 Matter Mater. Phys. **91**, 235419 (2015).
401 46. W. Li, Phys. Rev. B - Condens. Matter Mater. Phys. **92**, 075405 (2015).
402 47. P. A. George, J. Strait, J. Dawlaty, S. Shivaraman, M. Chandrashekhar, F. Rana, and M.
403 G. Spencer, Nano Lett. **8**, 4248 (2008).
404 48. K. Fukumoto, M. Boutchich, H. Arezki, K. Sakurai, D. Di Felice, Y. J. Dappe, K. Onda,
405 and S. Koshihara, Carbon **124**, 49 (2017).
406 49. Y. Anno, Y. Imakita, K. Takei, S. Akita, and T. Arie, 2D Mater. **4**, 025019 (2017).
407 50. O. Yamashita, S. Tomiyoshi, and K. Makita, J. Appl. Phys. **93**, 368 (2003).
408